Journal of Power Sources xxx (xxxx) xxx

Contents lists available at ScienceDirect

Journal of Power Sources

journal homepage: www.elsevier.com/locate/jpowsour

Effect of overcharge on $Li(Ni_{0.5}Mn_{0.3}Co_{0.2})O_2$/Graphite cells–effect of binder

Nancy Dietz Rago [a,*], Donald G. Graczyk [b], Yifen Tsai [b], Seema R. Naik [b], Jianlin Li [c,**], Zhijia Du [c], David L. Wood III [c], Leigh Anna Steele [d], Joshua Lamb [d], Scott Spangler [d], Christopher Grosso [d], Kyle Fenton [d], Ira Bloom [a]

[a] Chemical Sciences and Engineering Division, Argonne National Laboratory, Lemont, IL, 60439, USA
[b] Analytical Chemistry Laboratory, Chemical and Fuel Cycle Technologies Division, Argonne National Laboratory, Lemont, IL, 60439, USA
[c] Energy and Transportation Science Division, Oak Ridge National Laboratory, Oak Ridge, TN, 37831, USA
[d] Power Sources Technology Group, Sandia National Laboratories, Albuquerque, NM, 87185, USA

HIGHLIGHTS

- LFP/Graphite cells made with pVdF or CMC binders were overcharged to 100–250% SOC.
- Marked microstructural changes in the anode with SOC were seen in those with CMC.
- The number of organics in the SEI was sensitive to binder.

ARTICLE INFO

Keywords:
Lithium-ion battery
Overcharge
Microstructure
SEI
Anode
Binder

ABSTRACT

Cells based on NMC/graphite, containing styrene-butadiene rubber/carboxymethylcellulose binder in the anodes and pVdF latex/carboxymethylcellulose in the cathodes, were systematically overcharged to 100, 120, 140, 160, 180, 250% and 270% state-of-charge. The impact of the binder was characterized by elemental analysis, SEM, and HPLC. These results were compared to similar cells just using the poly (vinylidene difluoride) binder. Not only did the binder impact the rate of transition metal transport from the cathode to the anode, it also had a marked effect on the microstructure and composition of the materials on the anode surface.

1. Introduction

As the production of electric vehicles increases, limited battery life, safety concerns and cost have become important obstacles to the large-scale acceptance of lithium-ion (Li-ion) batteries by the public. Among the safety issues, overcharge is one of the most common and most hazardous problems associated with commercial Li-ion batteries. Because of the serious hazardous consequences of overcharge, the development of safe electric vehicle batteries will depend on a better understanding of the physical and chemical changes of overcharging. Thus, the understanding would be the first step to mitigate the effects of overcharging from the safety point of view.

Previously, we presented the results of our systematic study of the overcharge response of cells containing $Li(Ni_{0.5}Mn_{0.3}Co_{0.2})O_2$ cathodes, an electrolyte consisting of 1.2 M $LiPF_6$ in EC:DEC (3:7 by wt) and graphite anodes. Both the cathode and anode used poly (vinylene difluoride) (pVdF) binders. The results showed the effect of the extent of overcharge on the morphology and chemistry of the electrodes and the solid electrolyte interphase (SEI) layer.

In the present study, we continued our methodical approach to the work. Logically, one would expect that the constituents of the battery electrodes would influence the overcharge response. Argonne, Oak Ridge and Sandia National Laboratories collaborated to understand how changing, in this case, the binder would influence it.

The binder influences the cost and environmental impact of battery manufacture [1–3]. The binder plays an important role in the production and subsequent performance of the battery as it serves to connect and disperse the active materials and adheres the resultant slurry to the

* Corresponding author.
** Corresponding author.
E-mail addresses: dietz@anl.gov (N. Dietz Rago), lij4@ornl.gov (J. Li).

https://doi.org/10.1016/j.jpowsour.2019.227414
Received 1 August 2019; Received in revised form 3 October 2019; Accepted 5 November 2019
0378-7753/© 2019 Elsevier B.V. All rights reserved.

current collector. Poly (vinylidene fluoride) (pVdF) is currently the most commonly used binder in Li-ion batteries. pVdF was dissolved in N-methyl-2-pyrrolidone (NMP), which is volatile and toxic. Water-based alternatives, such as carboxymethylcellulose (CMC) and styrene-butadiene rubber (SBR), are being studied as alternatives to pVdF [3]. Comparable electrochemical performance has been demonstrated using electrodes made by aqueous processing and conventional organic solvent-based processing [4,5].

Small $LiNi_{0.5}Mn_{0.3}Co_{0.2}O_2$(NMC532)/graphite cells were made with SBR/CMC and latex/CMC binder for the graphite anode and NMC532 cathode, respectively. The cells were charged to 100, 120, 140, 160, 180 and 270% state-of charge (SOC). After overcharge, the cells were discharged to 0% SOC and subsequently disassembled in an argon-filled glovebox.

The point of the current study was to compare the changes caused by overcharging the above cells to that observed previously [6–8]. To facilitate the comparison, the two groups of cells will be referred to as NMP- and aqueous-processed. Since greater changes were seen on the anodes than on the cathodes in the previous study, most of the characterization work focused on the anodes in this work which showed the binder effect on overcharging, such as transition metal dissolution in the cathode and migration to the anode, and SEI properties in the anodes. As the binders in the cathode have little effect on the anode and vice versa, two sets of cells with different binders in the anode and cathode can provide a fair comparison without the need to expand into a matrix of 4. The microstructural changes on the surface of the anodes were characterized by scanning-electron microscopy. Chemical changes in the aqueous-processed overcharged anodes were measured by inductively coupled plasma mass spectrometry (ICP-MS), and high-performance liquid chromatography (HPLC).

2. Experimental

Similar experimental materials and procedures have been reported in our previous work [6–8]. The following description is mainly for the reader's convenience.

2.1. Materials

1.5-Ah Li-ion cells containing NMC532/graphite chemistry were fabricated, formed and overcharged, as described in a previous publication [6]. The cell information is listed in Table 1. The rated capacity corresponded to about 55% of the theoretical amount of lithium in the oxide. The NMC532 cathode and graphite anode contained the water-soluble binders. It should be noted that the copper foil had a shiny side and a rough, dull side. The smooth side was in direct contact with a roller during the electrodeposition process; the rough one faced the solution.

The NMC532 cathode was coated on an Al foil which was treated by corona treatment (4.4 J cm^{-2}) for superior slurry wetting on the substrate [9] following similar electrode fabrication reported in a previous publication [10]. The negative-to-positive ratio was 1.1:1. Except for the outer two layers, all electrodes were double-sided. The electrolyte consisted of 1.2 M $LiPF_6$ in ethylene carbonate:diethyl carbonate (EC:DEC) (3:7 by wt). Additional information is given in Ref. 4. The cells were formed by charging/discharging at the C/20 rate between 2.5 and 4.2 V for 4 cycles.

Table 1
Cell construction information.

	Compositions	Electrode size (loading)
Anode	Electrode: 92 wt% A12 graphite (ConocoPhillips), 2 wt% C-65 carbon black (Timcal), 4.8 wt% SBR (Targrey)/1.2 wt% CMC (Sigma Aldrich, $M_w = 250{,}000$; DS = 0.9) 35% porosity	86.4 mm × 58 mm (6.5 mg/cm^2)
Cathode	Electrode: 90 wt% $LiNi_{0.5}Mn_{0.3}Co_{0.2}O_2$ (TODA America Inc.), 5 wt% powder grade carbon black (Denka), 4 wt% pVdF Latex (Solvay Solef® XPH-859)/1 wt% CMC (Sigma Aldrich, $M_w = 250{,}000$; DS = 0.9) 35% porosity	84.4 mm × 56 mm (12.5 mg/cm^2)
Separator	Polypropylene–polyethylene–polypropylene (Celgard® 2325)	89 mm × 61 mm × 25 μm
Electrolyte	1.2 M $LiPF_6$ in EC:DEC (3:7 by weight, BASF)	–

After formation, the cells were shipped to SNL. The cells were then instrumented with thermocouples, voltage sense leads, and current-carrying cables; and fixtured in phenolic constraints. A Bitrode battery tester was used to carry out the overcharging as well as to discharge them after the overcharge test. A constant current charge rate of 1C (1.5A) was applied to the cells to reach the desired state of overcharge. Cells were set to 100% (no overcharge), 120%, 140%, 160%, 180%, and 270% SOC (failure, compliance voltage of 20 V met). The overcharge was followed by a 30-min rest and a discharge at the 1-C rate to 2.5 V. If the cell exceeded a voltage of 2.8V after a 30-min rest, then a subsequent discharge was performed. Depending on the level of overcharge, multiple discharges were performed in an attempt to remove capacity and reduce voltage in order to satisfy shipping requirements. The higher states of overcharge exhibited increased impedance so large polarization was seen with attempts to decrease the cell voltage for shipment. Once the 2.8V was met, the cell was monitored to understand voltage recovery. The cells were shipped to ANL in this state for post-test analysis.

2.2. Post-test characterization

In an argon-filled glovebox, the cells were opened using ceramic scissors. The electrodes were removed from the separator and allowed to dry. Sections of the positive and negative electrodes were cleaned two times by swirling 1 min each in excess dimethyl carbonate (DMC). The washed electrodes were used for elemental analysis (ICP-MS), HPLC and SEM analyses.

ICP-MS. In the glove box, the electrode coatings were scraped off the foils into polyethylene weighing dishes using a spatula. In the analysis process, each sample was first heated in air to burn off the carbon/organic components. For this step, a 100-mg portion of the sample material was transferred to a weighed quartz beaker (25 mL) and weighed. Then the beakers were placed in a laboratory furnace and heated in stages at 250, 500, and 700 °C. The temperature at each setting was held for several hours with at least 4 h at 700 °C to ensure the complete removal of the graphitic carbon. The beakers were cooled in air.

The residue from ignition was dissolved by adding to the quartz beakers a small amount of water (enough to wet the residue), 3 mL Optima Grade HCl, and 2 mL Optima Grade nitric acid; covering the beaker with a watch glass; and heating under reflux. Each resulting solution was quantitatively transferred to a polypropylene centrifuge cone and diluted with water to 50 mL. The anode solutions were analyzed with a PerkinElmer/Sciex ELAN DRC-II ICP-MS to determine concentrations of Ni, Mn, and Co, using either scandium or indium as the internal standard. The inductively coupled plasma mass spectrometer (ICP-MS) was calibrated with solutions prepared by diluting spectroscopic standards procured from Ultra Scientific, North Kingstown, Rhode Island. The mass fraction (μg/g) of each element in the anode material was calculated using the element concentration, the volume of solution in which the sample was dissolved, and the mass of sample taken. Uncertainty in the reported values is assigned as the larger of ±1 μg/g or ±6% of the reported value.

The LINEST function in Microsoft® Excel® was used to fit the equation, $y = A\exp(bx)$, where y is the concentration of metal in solution (ppm by wt) and x is the %SOC, to the elemental analysis data. As written, the equation is not linear. It was linearized by taking the natural logarithm of both sides. The linear equation, $\ln(y) = \ln(A) + bx$, was then used by the LINEST function to generate the fits.

SEM. Pieces of electrode samples were placed in an airtight holder, based on the design published by ORNL [10]. After mounting the sample, the sealed holder was removed from the glovebox and evacuated. After evacuation, the lid screws were removed and the holder was placed in a JEOL JSM-6610LV scanning electron microscope (SEM). In the SEM column, the holder lid opened when the vacuum in the column exceeded the vacuum inside the holder. Energy-dispersive spectroscopy (EDS) was performed using an Oxford Instruments X-Max^N detector (detector size = 50 mm^2) and AZtecEnergy® software.

HPLC. Samples for HPLC analysis were prepared by scraping the anode coating (~40–70 mg) off the copper foil from the cells. The scrapings were placed in scintillation vials, then covered and removed from the glove box. Approximately 1–1.5 mL of HPLC-grade water (Sigma-Aldrich) and ~20–30 mg reagent-grade Na_2CO_3 were added to each vial. Na_2CO_3 was added to neutralize any nascent HF formed during this step.

In some cases, a small number of bubbles formed, indicating the presence of residual lithium. The contents of each vial were mixed thoroughly using a vortex mixer after the bubbling (if any) stopped. Approximately 2–2.5 mL CH_2Cl_2 (Sigma-Aldrich; Chromasolv®) was added to each vial. Again, the contents of each vial were blended thoroughly using the vortex mixer. After the layers separated, the bottom layer was carefully removed using a pipette. It was placed in another scintillation vial and allowed to dry overnight. The residue was then taken up in ~0.5 mL acetonitrile (HPLC grade), placed in an amber HPLC vial, and capped. The sample vials were placed in the autosampler.

HPLC analyses were performed using an Agilent Technologies 1260 Infinity chromatograph equipped with an auto-sampler (Agilent Technologies G1329B); a quaternary pump (Agilent Technologies G1311B); and an electrospray, quadrupole mass spectrometer detector [Agilent Technologies 6120; mass spectrometer (MSD)]. The fragmenting voltage in the MSD was 70 V and data were collected in the range of 50–1000 Da. Separations were performed using a Zorbax® ODS column (5 μm, 4.6 × 250 mm), which was thermostated at 25 °C. Water and acetonitrile (both HPLC-grade, Sigma-Aldrich, and containing 0.1% formic acid) were mixed in a 60/40 v/v ratio using the quaternary pump to form the mobile phase. The pumping speed was 1 mL min^{-1}. The column was purged with the mobile phase for 5–10 min before using.

HPLC data reduction and calculations. The data in a selected region were used to construct single-ion chromatograms. A tolerance band of −0.7 to +0.3 Da around the selected values was used. The data were categorized in terms of mass and total abundance; the computer-based method for this is given below in pseudocode.

Create table indexed on mass.
Find start and end times to define selected region.
For each mass in region.

Is mass in the mass table?
Yes: add abundance to current abundance value for the given mass.
No: add mass and abundance to table.

Create list of (mass, abundance) pairs.
Sort list on abundance (maximum to minimum).
Read top 15 most-*abundant masses from sorted list.*

Create abundance vs. time profiles for the masses from the original data using most-abundant masses.

The mass spectra were calculated from these abundance vs. time profiles and the raw MSD data using some of the principles described by Malinowski [11a]. The mathematics are described in more detail in the supplemental material. Theoretical mass spectra in the molecular ion region were calculated using IsoPro 3.1 [11b].

3. Results and discussion

The cells were charged at the C/1 rate until the desired capacity had been reached. The charging was performed at 30 °C. The end of charge voltage as a function of state of charge is shown in Table 2, which are the same as reported in Ref. 4. It should be noted that, at 270% SOC, the voltage was limited by the power supply.

Based on the visual inspection of the anode surfaces during disassembly (see Fig. S1 in the Supplemental Material), it was immediately apparent that the NMP-processed anode surfaces appear to have reacted more based on the degree of surface discoloration remaining after DMC rinsing. At 140% SOC, there was evidence of "pull out" of anode surface onto the separator during disassembly in both NMP and aqueous-processed anodes, however, there was substantially more of this happening in the NMP-processed cell, suggesting that binder adhesion was breaking down more in the NMP-processed cell. By 180% SOC both surfaces visually appeared similar and delamination occurred easily in both electrodes with handling during disassembly. At 270% SOC, the active material of the aqueous-processed cell stuck to the separator in some cases.

ICP-MS. The results from elemental analysis are given in Table 3. The amount of each element tended to be approximately constant until about 160% SOC. After that SOC, the weight fractions increase dramatically. It was interesting to note that the amount of phosphorus was about two to three times that of each metal in most cases. A plot of these values is shown in Fig. 1.

Recasting the transition metal data in terms of mole fraction yielded the last column in Table 3. The ratios of metals are the same as the cathode, within experimental error, indicating all the metals were transported to the anode equally, like that seen earlier (Table 4) [7].

Comparing these results to those found in the earlier study [7] (see Table 4 and Fig. 1) showed that the amounts of transition metal that they were about the same up to 120% SOC. Thereafter, the amounts in the aqueous-processed tended to be smaller, except in the case of Mn at 180% SOC. Here, it was markedly larger for an as-yet unknown reason.

Insights into the mechanisms responsible for metal migration were obtained by least-squares fitting of the equation, $y = Ae^{bx}$, to the data from both sets of cells. As shown in Fig. 1, $y = Ae^{bx}$ represented the data well ($r^2 > 0.95$) in the NMP-processed case and poorly in the aqueous-processed one, indicating that the binder influenced the rate of metal migration during overcharge. The phosphorus data were too complex to be well-represented by simple equations.

SEM. A baseline comparison of the pristine electrodes showed that the anode microstructure in both processes appeared similar; however, at higher magnification, the carbon black in the aqueous-processed anode was more uniformly dispersed, whereas in the NMP-processed anode the carbon black was aggregated. In addition, adhesion to the current collector was much stronger in the aqueous-processed electrodes in comparison to the NMP-processed electrodes. Stripping the NMP-processed anode surface with sticky tape resulted in the clean removal of the active surface from the collector, whereas in the aqueous anode, the removal was difficult and residual active material still remained on the collector. Fig. 2 shows the pristine anode surfaces and the collector after mechanical removal of the active material. Both of these observations provide evidence that the SBR/CMC binder produces a more

Table 2
Cell voltages as a function of %SOC.

%SOC	Cell voltage, V
100	4.2
120	4.78
140	5.75
160	5.78
180	6.86
270	20

Table 3
Elemental analysis results from the aqueous-processed anodes.

	Concentration, ppm by wt				Transition metal molar ratio
%SOC	Mn	Co	Ni	P	Mn:Co:Ni[a]
100	16	12	35	2044	0.29:0.19:0.54
120	10	6.4	20	1724	0.27:0.17:0.55
140	34	14	50	2360	0.36:0.14:0.50
160	111	70	191	1763	0.31:0.18:0.50
180	4186	244	738	4186	0.34:0.16:0.49
270	2340	1354	3603	16317	0.34:0.18:0.48

[a] The sum of these values may not equal to 1.00 in all cases due to rounding.d.

Table 4
Elemental analysis results from overcharged, NMP-processed anodes from Ref. [5].

	Concentration, ppm by wt				Transition metal molar ratio
%SOC	Mn	Co	Ni	P	Mn:Co:Ni[a]
100	16.4	8.37	21.5	1730	0.37:0.18:0.45
120	33.8	17.4	55.6	1370	0.33:0.16:0.51
140	221	144.4	479	1210	0.27:0.17:0.56
160	499	236	772	2050	0.35:0.15:0.50
180	1610	937	2750	6140	0.32:0.17:0.51
250	3500	2610	6580	10800	0.29:0.20:0.51

[a] The sum of these values may not equal to 1.00 in all cases due to rounding.

uniform slurry and stronger attachment to the collector.

The NMP- and aqueous-processed anode surfaces of the 120, 140 and 160% SOC cells are shown in Fig. 3. At 120% SOC, the NMP-processed anode microstructure did not show a discernible difference from that of the 100% SOC electrode. However, the graphite particles in the aqueous-processed anode (120% SOC) were covered with a discontinuous SEI film that appeared to contain small embedded particles. In some areas, isolated dendrites were starting to appear in both types of anodes.

By 140% SOC, pull-out onto the separator was evident in both cells. The abundance of dendrites in both processes indicates that extracted Li from the cathode is depositing on the anode surface faster than the kinetics of graphite intercalation. In the NMP-processed cell, the dendrites were present as either smooth or heavily coated. The coated dendrites contained nanoscale particles of the transition metals. For an explanation as to why some dendrites were smooth and some heavily coated, the reader is referred to a previous publication [6] that describes in more detail the evolution of microstructures in the systematically overcharged NMP-processed cell. Transition metals were not yet detected in the aqueous-processed anode surface, and the dendrites were smooth, an indication that fewer electrolyte decomposition reactions were occurring and that the cathode was more stable than its NMP-processed counterpart. The dendrites appeared partially matted down in the underlying solid electrolyte interphase (SEI) layer. The relatively high concentration of F associated with the aqueous-processed anode substantiates the composition of the SEI layer, which contained LiF, a major component in systems that contain $LiPF_6$ salts [12–14].

At 160% SOC, both anode surfaces had a dense concentration of dendrites, with the NMP-processed dendrites being heavily coated, while the dendrites on the aqueous-processed anode were smooth. Transition metals were detected on the aqueous-processed surface at this point; however, the concentration was lower than that on the NMP-processed anode (see Fig. S2).

Delamination of the active material from the collector was evident in the NMP-processed anode, while the aqueous-processed anode was still intact. This difference could be attributed to an early onset of binder breakdown in the NMP-processed anode and the subsequent loosening of the bond between the collector and the active material layer.

A dramatic deviation in the surface microstructures between the NMP- and aqueous-processed anodes was seen at 180% SOC. At this SOC, the NMP-processed anode was considerably more reacted with areas of complex layered microstructures and more delamination from the collector. This may be an indication that the reactions between the

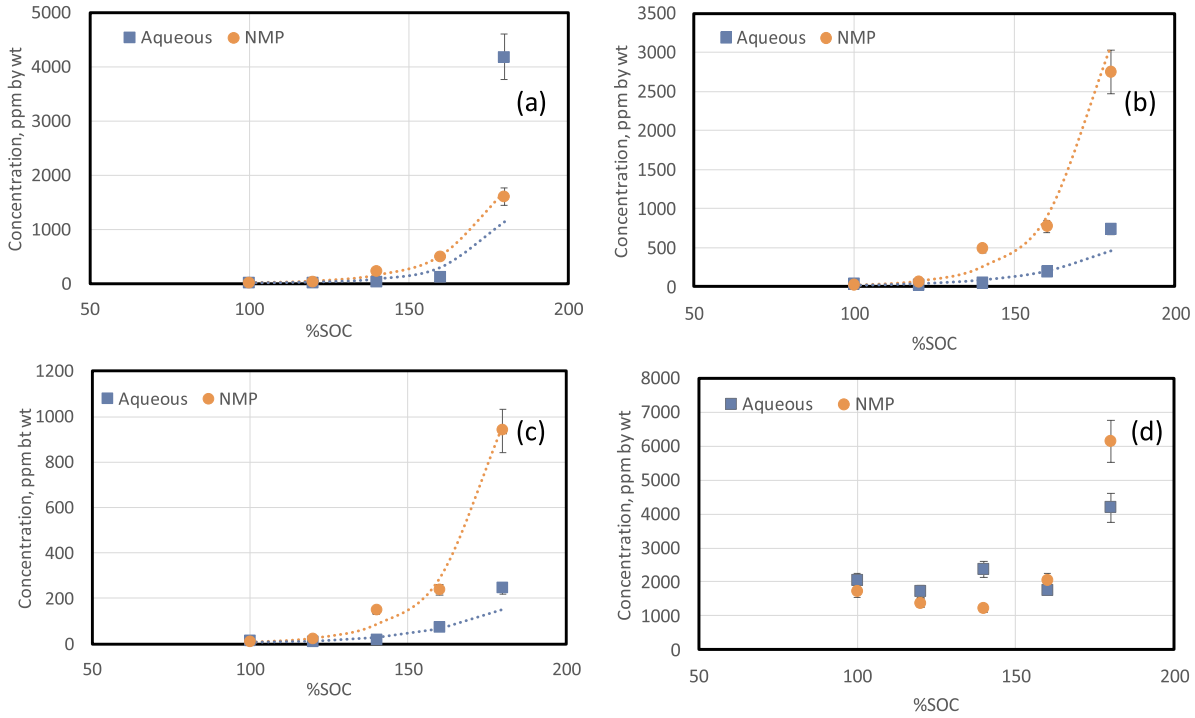

Fig. 1. Concentration vs. %SOC for (a) Mn, (b) Ni, (c) Co and (d) P. The values from the failed cells were not included due to cell venting. The error bars represent ±10% uncertainty in the reported values. If the error bar is not visible, then it was smaller than the marker. The dotted lines represent the results of linear, least-squares fitting of $y = Ae^{bx}$ to the transition metal data. The values of the fitting coefficients and the regression coefficient, r^2, are given in the Supplemental Material.

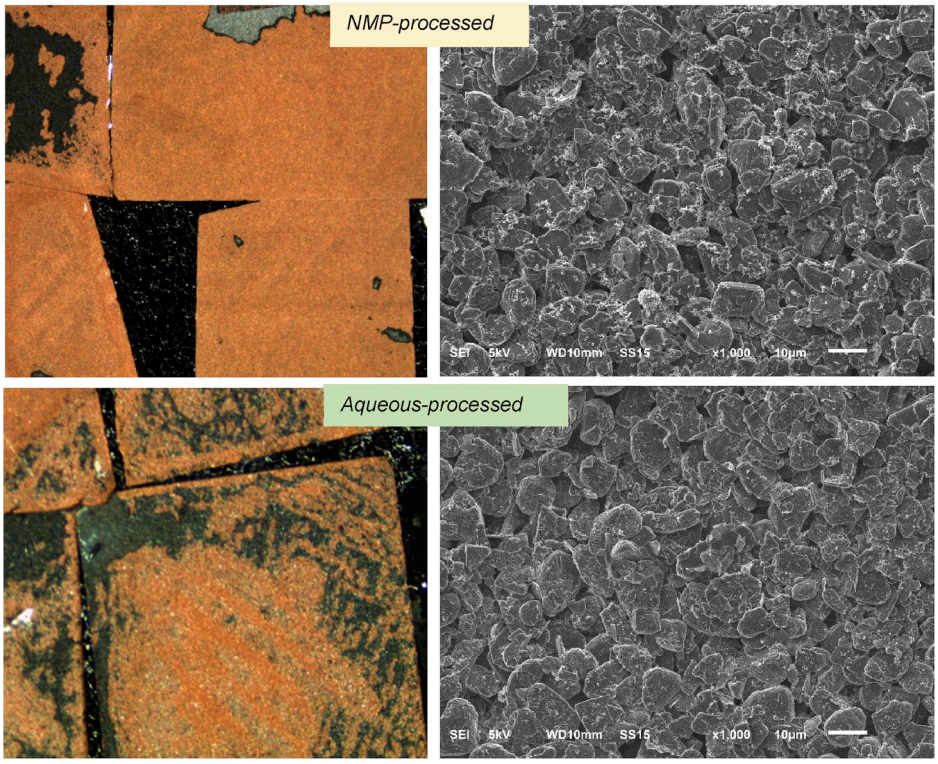

Fig. 2. Pristine NMP-process and aqueous-processed anode surfaces. Color images show anodes stripped of overlying active material. (For interpretation of the references to color in this figure legend, the reader is referred to the Web version of this article.)

anode and electrolyte were occurring faster and were more exothermic. In an overcharge study conducted by Yuan et al. [15], ICP analysis was used to measure the relationship between Li content in $Li(Ni_{0.33}Co_{0.33}Mn_{0.33})O_2$ and SOC in a cell with carbonaceous microspheres as the anode. Their results show a nearly linear decrease in Li with increasing SOC until 180% SOC. After 180% SOC, very little Li was detected. They surmise that after 180% SOC, it was difficult to remove the remaining Li in the cathode, consequently electrolyte decomposition and side reactions dominantly affect capacity. These results represent a turning point in overcharge reaction trends that could be manifested by the type of microstructural changes seen here at 180% SOC. New surface species in addition to the sequence of reactions now further complicate the surface film morphology, resulting in multilayer structures [16,17] and a corresponding nonuniform current distribution associated with Li deposition/dissolution [17]. Fig. 4 shows an area of layered microstructures and the corresponding EDS data. Transition metal concentration is highest in the dendrite layer (layer 3) followed by the superficial layer (layer 1).

An SEM montage of an area with a layered microstructure and the corresponding EDS data is shown in Fig. 4. This unique perspective was possible due to pull-out of some anode material onto the separator during disassembly. The gouged out region had sloped walls, exposing the various layers in a step-wise manner as seen in this image. This was not a common feature along the anode surface. Some areas had fewer layers. Transition metal concentration was highest in the dendrite layer (layer 3) followed by the superficial layer (layer 1).

The corresponding 180% SOC aqueous-processed anode surface is shown in Fig. 5. Delamination is now evident, but not to the extent seen in the NMP-processed anode. The surface exhibited charging on exposure to the electron beam, indicating the presence of insulating material on the surface, possibly the binder or insulating reaction layer.

The aqueous anode surfaces in Fig. 5 are from the dull side of the collector. The smooth-side surface microstructure was very similar. Layered structures were not found. Most of the surface was covered by dendrites that had a different morphology depending on whether they were on the "white" or "black" region as annotated in Fig. 5. The white regions were covered with the typical dendrite structure, with some regions being matted down as seen at lower SOC. The black regions had a more rounded nodular dendrite structure. The emergence of the more nodular morphology is an indication that temperature, current density and electrolyte composition are changing with increasing SOC [18,19]. Transition metals were detected in both regions; however, in some of the white areas, transition metals were not detected. These areas could represent areas of pull-out onto the separator, in which case EDS analysis was not done on the true surface. It is also possible that transition metals were not uniformly distributed across the surface for a few reasons such as local variations in current density, concentration of electrolyte salt, or electrical disconnection from the current collector.

The NMP-processed cells were charged up to 250% SOC, at which point the cell vented whereas the aqueous-processed cells were charged up to 270% SOC and failed. The microstructure in both cells is dominated by coated dendrites (see Fig. S3). Transition metals are detected on both surfaces in association with dendrites and the SEI layer, with the SEI layer having the highest concentration. There is significant pull-out of the active material onto the separator in both cells, making microstructural spatial relationships extremely difficult to establish. Extensive delamination of the active layer from the collector is possible evidence that moisture and oxygen released from electrolyte decomposition and structural deformation of the cathode have increased [15].

HPLC. Samples of anode material were hydrolyzed, as described above, to gain an understanding of the concentration and nature of the organics on the surfaces. All total ion count vs. time plots were similar; the intensities of the peaks changed with the extent of overcharge. Fig. S4 in the Supplemental Material shows the total ion count vs. time data from the HPLC experiments.

Using a blank sample (acetonitrile only) showed that the peak at ~2.3 min was an artifact from the column and was removed from further consideration. Only two peaks in the chromatogram showed a

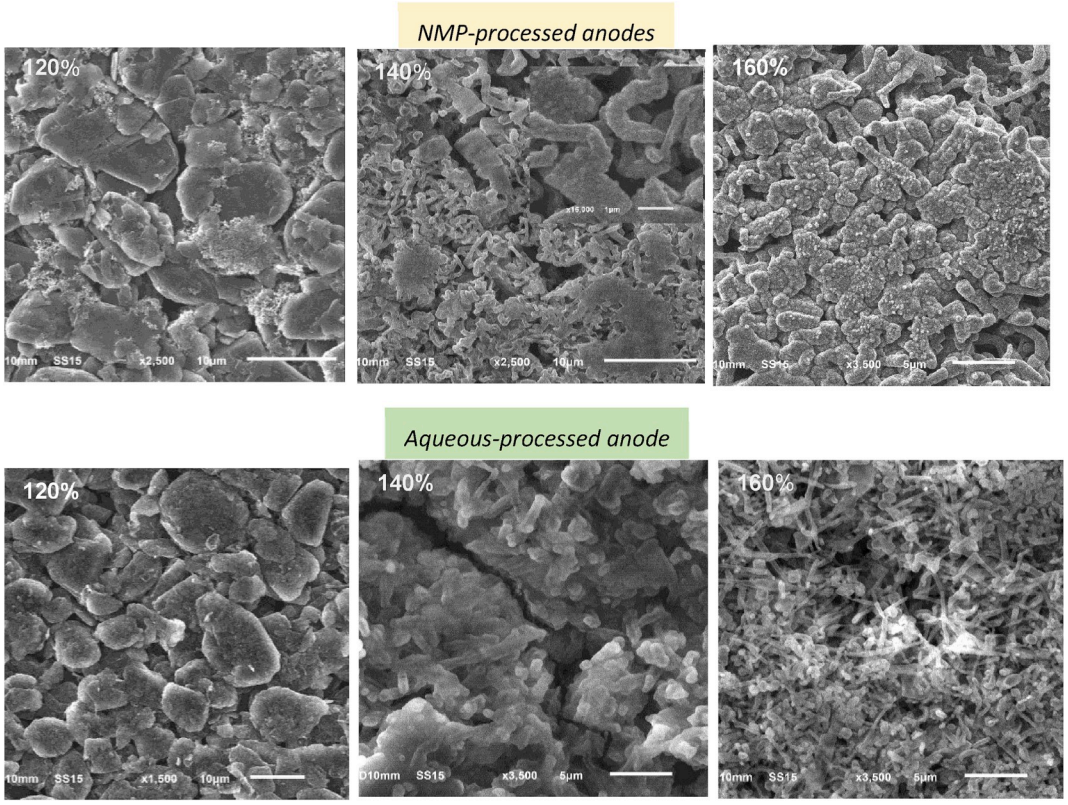

NMP	120% SOC	140% SOC dendrites	160% SOC dendrites	160SOC SEI
C	91.28	57.19	34.00	28.79
O	5.14	30.81	23.21	33.93
F	3.34	9.97	27.71	31.81
Na				
Si		0.09	0.13	
P	0.05	0.48	1.65	4.05
S		0.35	0.38	0.33
Mn		0.41	2.58	0.52
Co		0.17	3.07	0.22
Ni		0.55	7.04	0.48
Cu	0.19	-0.03	0.23	-0.13

Aqueous	120% SOC	140% SOC dendrites	160% SOC dendrites
C	86.72	56.40	67.96
O	3.56	11.04	15.54
F	9.40	30.92	15.22
Na			
Si		0.03	0.14
P	0.35	1.50	0.56
S		0.08	0.05
Mn			0.12
Co			0.04
Ni			0.14
Cu	-0.03	0.02	0.22

Fig. 3. NMP- and aqueous-processed anodes at 100, 140 and 160% SOC and corresponding EDS. data. Transition metals are detected earlier in the NMP-processed cells (140% SOC) in comparison to the aqueous-processed cells (160% SOC).

dependence on the %SOC, ~2.7 and ~6.5 min.

From the data shown in Fig. S4 (see Supplemental Material), the background level was very high in all samples. To isolate the true mass spectra from the background, single-ion chromatograms, such as those shown in Fig. S5a for the first peak, were constructed for the 15 most common ions in the region around a peak using a simple computer search algorithm. Examining the results of the calculation (see Fig. S5a) shows that two ions, 199 and 221, displayed the same time dependency as the original peak centered around 2.7 min. The ion count vs. time profile for m/e = 199 was then used to calculate a crude mass spectrum using the least-squares methods described in Ref. 5. The results of these calculations are shown in Fig. 6.

From these results, the same material is present in the 100 and 120% SOC samples (retention time ~6.5 min; m/e = 63 Da). At 140% SOC, a new material appears at about 2.7 min (m/e = 419 Da). The 6.5-min retention time peak shifted slightly at 160% SOC to ~6.2 min (m/e = 387 Da), indicating a new compound was present, before shifting back to the original retention time of ~6.5 min (m/e = 563). The reason for this is not known.

An estimate of the number of carbon atoms was obtained from the ratio of the areas of *m* and *m*+1 peaks. Table 5 shows the range in values found in the calculation along with the observed value of the apparent molecular ion and the estimated uncertainty at the 95% confidence level. Taking the first entry as an example, the species may have between 10 and 15 carbon atoms in it.

It was assumed that the found products would be based on fragments of the organic solvent system and the $LiPF_6$ salt. Thus, the proposed compounds would be limited to combinations of $–OCH_2CH_2O-$ and $–OCH_2CH_3$ with PF_3 or $O{=}PF_3$. If the electrolyte fragments reacted with PF_3, one would expect a phosphite; if with the phosphorus oxyfluoride, a phosphate. However, the oxidation of a phosphite to phosphate could also easily have occurred during the sample preparation process. Organophosphates consisting of electrolyte fragments have been reported in the literature [20a-c]. Carbon-carbon double bonds were limited to cases where there are no other alternatives that made chemical sense. The proposed compounds can be protonated, due to the formic acid in the mobile phase in the HPLC, or sodiated (Na^+) from the Na_2CO_3 used in the experimental procedure. The proposed formulae for the compounds corresponding to the mass spectra in Fig. 6 are given in Table 6.

Comparing these results with the HPLC results in the pVdF-

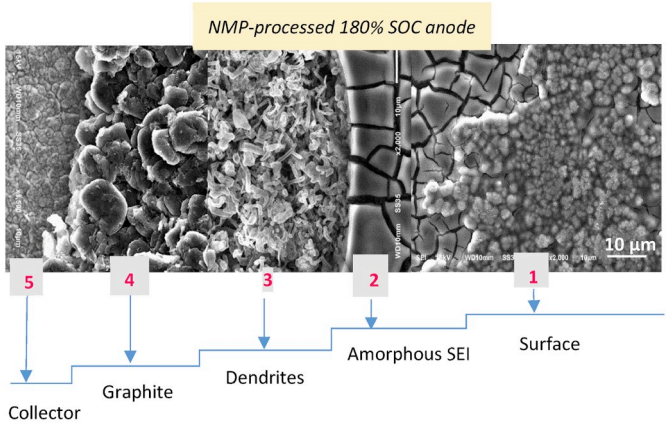

area	C	O	F	P	S	Mn	Co	Ni	Cu
1	42.25	32.48	11.45	2.06	0.13	0.96	3.76	6.69	
2	23.63	14.44	54.37	6.06	0.33	0.37	0.25	0.70	
3	45.09	32.48	9.50	1.65	1.20	1.20	3.33	6.28	
4	89.41	5.57	4.75	4.75					0.05

Fig. 4. 180% SOC NMP-processed anode and corresponding EDS data. This image captures a step-wise view of the anode from the surface down to the collector. Transition metal concentration is the highest in the topmost layer (1) and in the dendrite layer (3) [6].

containing cells shows that there are more potential compounds when using the CMC/SBR binder, 2 vs. 3, respectively. The compounds from the CMC/SBR cells tended to be higher molecular weight polymers and contain more phosphorus and fluorine than those from the other cells.

Plotting the relative areas of the m/e peaks against %SOC produces Fig. 7. The plot shows that the two major constituents, 419 and 563 Da, generally, tended to reach a constant area ratio.

The above results show that the effect of the binder is complex. The binder affects the composition and structure of the materials on the anode surface. Because the results show a dependence on the extent of overcharge, the discussion will be limited to what can happen during charging.

By comparing the elemental analysis results of the NMP- and aqueous-processed cells, one can see that the cathode binder affected the concentrations of the transition metals found at the anode and the apparent mechanism that caused dissolution and migration. There are published reports that aqueous-based binders cause aluminum corrosion [21–23]. Based on this, one may expect that the aqueous binder also enhances oxide corrosion, leading to more transition metals depositing on the graphite electrode. However, this was not observed. Quite the contrary, using the aqueous binder produced graphite electrodes with less metal.

A fundamental property that could cause these observations is how well the binder coated or adhered to ("wet") the oxide particles. We can assume that the surface of the oxide consists of metal ions with oxygen nearest neighbors, producing a polar surface. The CMC component in the binder (see Fig. 8) contains polar hydroxyl groups which may more readily lend themselves to adhering to a polar surface and coating it than the organic soluble, and relatively nonpolar, pVdF. A similar argument could be made for the relative wetting properties of SBR.

The SEM and HPLC results show the impact of the binder on the surface microstructure and chemistry on the anode. From the SEM results, the anodes from the aqueous-processed cells were less affected by overcharging than those containing pVdF. The surface microstructure of the aqueous-processed materials appeared to be have fewer decomposition products on the surface.

Comparing the HPLC results with those that were observed in the pVdF binder-containing electrodes [7] showed the impact of the binder to affect the course of the reactions to form SEI components. In the pVdF case, there were only two compounds with the proposed formulae $C_{16}H_{36}O_{10}P^{+}$ (FW = 419.42 g mol^{-1}) and $C_{13}H_{39}O_{11}P_2Na^{+}$ (FW = 445.29 g mol^{-1}). Initially, only the first compound was present. The concentration of the second compound increased at 140% SOC. The

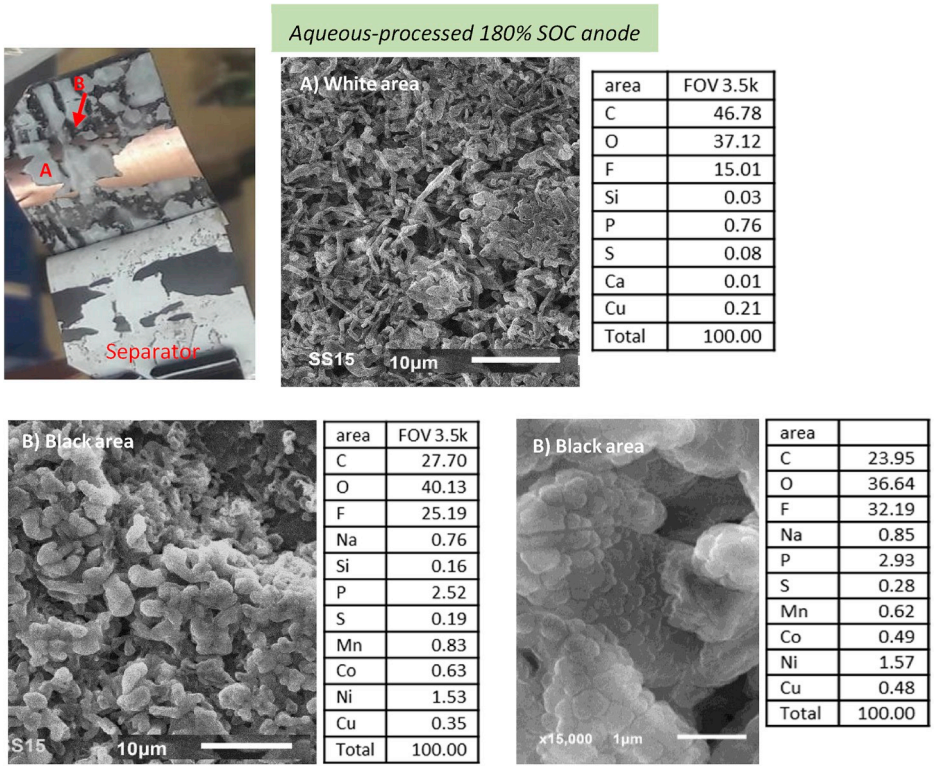

area	FOV 3.5k
C	46.78
O	37.12
F	15.01
Si	0.03
P	0.76
S	0.08
Ca	0.01
Cu	0.21
Total	100.00

area	FOV 3.5k
C	27.70
O	40.13
F	25.19
Na	0.76
Si	0.16
P	2.52
S	0.19
Mn	0.83
Co	0.63
Ni	1.53
Cu	0.35
Total	100.00

area	
C	23.95
O	36.64
F	32.19
Na	0.85
P	2.93
S	0.28
Mn	0.62
Co	0.49
Ni	1.57
Cu	0.48
Total	100.00

Fig. 5. 180% SOC aqueous-processed anodes and EDS data. Transition metals are detected in the heavily coated dendrites, seen as the black area (B) on the electrode.

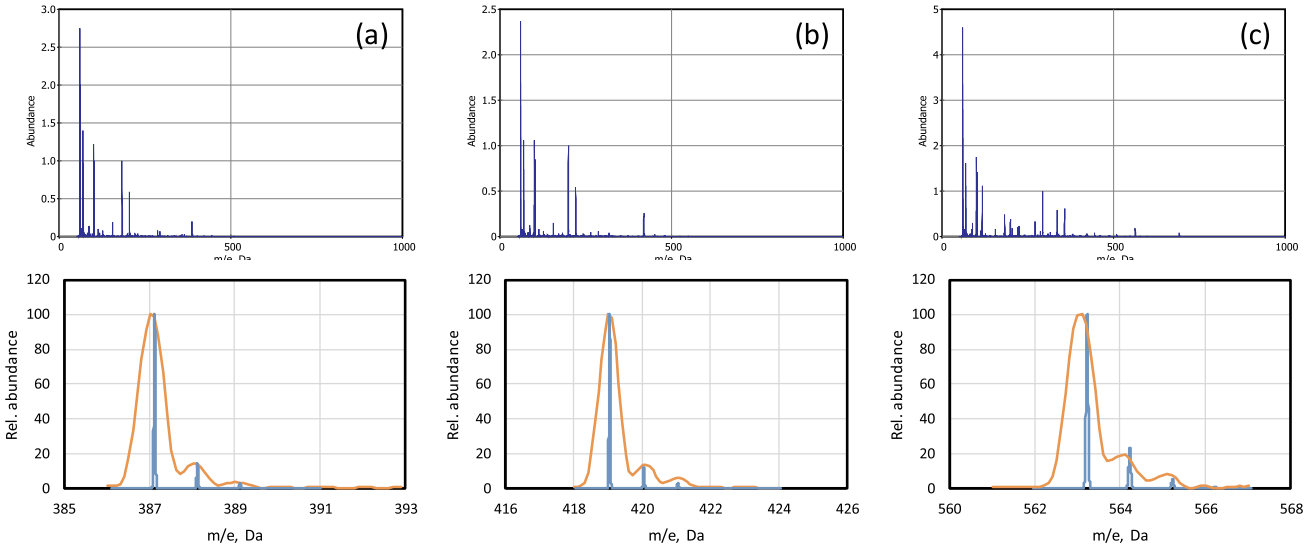

Fig. 6. Calculated mass spectra using the data shown in Fig. 5. (a) m/e = 387 Da; (b) m/e = 419 Da; and (c) m/e = 563 Da. The top row shows the total mass spectrum calculated from the experimental data. The bottom row shows the comparison of the experimentally-derived spectrum in the molecular ion region (orange) to that calculated from the natural abundance of the elements and their isotopes in the formulae given in Table 5 (blue). The theoretical mass spectra in the molecular ion region are shown in Fig. 6 also. Comparing the experimentally-derived results with those derived from the natural abundance of the isotopes shows that they agree fairly well. The discrepancy in peak positions between the theoretically- and experimentally-derived is about 0.1 Da. The formulae proposed in Table 5 are, therefore, reasonable approximations of the actual species. . (For interpretation of the references to color in this figure legend, the reader is referred to the Web version of this article.)

Table 5
Estimated number of carbon atoms and found values of m/e from the mass spectra shown in Fig. 4.

Apparent m/e value	Estimated number of carbon atoms from mass spectrum (2σ)[a]
419	12.4 (2.6)
387	12.6 (2.1)
563	19.0 (2.2)

[a] 95% confidence level.

two compounds tended to reach a constant area ratio.

In the aqueous binder case there were three, and the relationship between two of them, 419 and 563 Da, was like that described above. The relationship between the 387 Da species and the others is not clear currently.

It is interesting to note that there was a proposed compound in the pVdF case that had, approximately, the same molecular weight as that in the aqueous binder case, $C_{16}H_{36}O_{10}P^+$ and $C_9H_{22}O_{12}P_2Na^+$, respectively. The apparent differences between them are the number of carbon and phosphorus atoms. Based on only the molecular weight information, one may think that these may be the same molecule. However, the ratio of the areas of the m and $(m + 1)$ peaks was sufficient to denote them as distinct compounds. This is an example of how the binder can influence the number of carbon atoms in the compound as well as the number of heteroatoms.

Table 6
Proposed formulas for compounds corresponding to the mass spectra in Fig. 6 and their calculated formula weights.

Mass spectrumlabel in Fig. 6	Proposed formula	Calc'd formula weight, g mol^{-1}
A	[FP(=O) $(OCH_2CH_2OCH_2CH_2OCH_2CH_2OH)_2]Na^+$	387.29
B	[$(HOCH_2CH_2O)_2P$ (=O)$OCH\overline{}CHOP$(=O) $(HOCH_2CH_2O)_2]Na^+$	419.22
C	[FP(=O) $((OCH_2CH_2)_5OH)_2]Na^+$	563.50

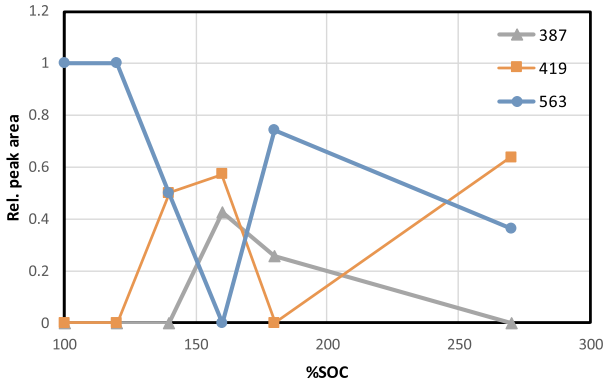

Fig. 7. Relative peak areas of the molecular ion peak vs. %SOC. The numbers in the legend represent the weight of the molecular ions in Daltons.

Examining the differences in the binders can provide a rationalization of the above observations. The first binder, pVdF, is a fluorinated hydrocarbon, which can be represented as $-(CH_2CF_2)_n-$. On the other hand, CMC is a polysaccharide, schematically shown in Fig. 6. The differences in reactivity patterns may reflect the interaction of some of the nascent lithium with the binder. In the pVdF case, there are not many low-energy reaction pathways available. The only ones possible would

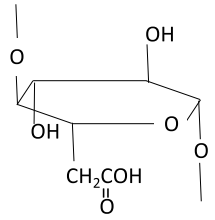

Fig. 8. Schematic of the repeating unit in CMC.

entail breaking C–C, C–H, or C–F bonds, which may not be energetically possible in the battery system.

The structure of CMC lends itself to easily conceivable reactions with lithium. The most obvious ones are the reactions of the carboxyl and hydroxyl groups to form lithiated analogs, such as –C (=O)O–Li^+ and –C-O^-Li^+. Thus, in the CMC case, there may be at least two competing reaction pathways for the nascent Li on the electrode surface, one with the binder and the other with the electrolyte. For pVdF, there would be fewer.

4. Conclusion

Cells based on NMC/graphite, containing water-soluble binders in the positive and negative electrodes, were systematically charged to 100, 120, 140, 160, 180, and 270% SOC. Scanning electron microscopy and EDS of the anodes revealed several SOC-dependent trends. Dendrites appeared at 120% SOC in both types of cells and progressively grew with increasing SOC; however, the concentration of dendrites was greater in NMP-processed cells. The aqueous-processed anodes had less evidence of microstructural degradation as a function of increasing SOC. Given that the differences in microstructure and transition metal concentration between the two binders can be the result of local variations in current density or electrical disconnection from the current collector, it would appear that the binder in the aqueous-processed anode was mitigating these effects by providing better adhesion to the collector, a more uniform distribution of electrode components in the slurry and possibly a more stable SEI layer.

Characterization of the anodes by ICP-MS, and HPLC showed several extent-of-overcharge-dependent trends also. Comparing these results to those obtained from NMP-processed cells containing the pVdF binder showed the effect of the binder on an abuse response. The negative electrodes containing the CMC binder displayed less damage. Three organic reaction products were observed in both cases. Two of those in the pVdF case tended to a constant ratio; all three did so in the CMC case. The reaction products changed from polyethers to organophosphates when the binder was changed from pVdF to CMC.

Declaration of competing interest

The authors declare that they have no known competing financial interests or personal relationships that could have appeared to influence the work reported in this paper.

Acknowledgments

We gratefully thank the U.S. Department of Energy (DOE), Office of Energy Efficiency and Renewable Energy, Vehicle Technologies Office for supporting the work at Argonne. Argonne National Laboratory is operated for DOE Office of Science by UChicago Argonne, LLC under contract number DE-AC02-06CH11357.

The work at Oak Ridge National Laboratory, managed by UT Battelle, LLC for the DOE under contract DE-AC05-00OR22725, was sponsored by the DOE's Office of Energy Efficiency and Renewable Energy, Vehicle Technologies Office, Applied Battery Research.

Sandia National Laboratories is a multi-mission laboratory managed and operated by National

Technology and Engineering Solutions of Sandia, LLC, a wholly owned subsidiary of Honeywell International, Inc., for the DOE's National Nuclear Security Administration under contract DE-NA0003525.

The U.S. Government retains for itself, and others acting on its behalf, a paid-up nonexclusive, irrevocable worldwide license in said article to reproduce, prepare derivative works, distribute copies to the public, and perform publicly and display publicly, by or on behalf of the Government.

Appendix A. Supplementary data

Supplementary data to this article can be found online at https://doi.org/10.1016/j.jpowsour.2019.227414.

References

[1] D.L. Wood III, J. Li, C. Daniel, J. Power Sources 275 (2015) 234–242.
[2] M. Osinska-Broniarz, A. Martyla, L. Majchrzycki, M. Nowicki, A. Sierczynska, Eur. J. Chem. 7 (2) (2016) 182–186.
[3] R. Wang, L. Feng, W. Yang, Yinyin Zhang, Yanli Zhang, W. Bai, B. Liu, W. Zhang, Y. Chuan, Z. Zheng, H. Guan, Nanoscale Res. Lett. 12 (2017) 575.
[4] Zhijia Du, Rollag Kelsey, Jianlin Li, Seong Jin An, Marissa Wood, Yangping Sheng, Partha Mukherjee, Claus Daniel, David Wood, J. Power Sources 354 (2017) 200–206.
[5] David Wood, Jeffrey Quass, Jianlin Li, Shabbir Ahmed, David Ventola, Claus Daniel, Dry. Technol. 36 (2018) 234–244.
[6] N. Dietz Rago, J. Bareno, J. Li, Z. Du, D.L. Wood III, L.A. Steele, J. Lamb, S. Spangler, C. Grosso, K. Fenton, I. Bloom, J. Power Sources 385 (2018) 148–155.
[7] I. Bloom, J. Bareno, N. Dietz Rago, F. Gogan, D.G. Graczyk, Y. Tsai, S.R. Naik, S.-D. Han, E. Lee, Z. Du, Y. Sheng, J. Li, D.L. Wood III, L.A. Steele, J. Lamb, S. Spangler, C. Grosso, K. Fenton, J. Power Sources 385 (2018) 156–164.
[8] J. Bareno, N. Dietz Rago, F. Dogan, D.G. Graczyk, Y. Tsai, S.R. Naik, S.-D. Han, E. Lee, Z. Du, Y. Sheng, J. Li, D.L. Wood III, L.A. Steele, J. Lamb, S. Spangler, C. Grosso, K. Fenton, I. Bloom, J. Power Sources 385 (2018) 165–171.
[9] J. Li, C. Rulison, J. Kiggans, C. Daniel, D.L. Wood III, J. Electrochem. Soc. 159 (2012) A1152–A1157.
[10] J. Li, C. Daniel, S.J. An, D.L. Wood III, MRS Advances 1 (2016) 1029–1035.
[11] (a) E.R. Malinowski, Factor Analysis in Chemistry, third ed., John Wiley and Sons, Inc., New York, 2002;
(b) IsoPro 3.1 is available, https://sites.google.com/site/isoproms/.
[12] S.J. An, J. Li, C. Daniel, D. Mohanty, S. Nagpure, D.L. Wood III, Carbon 105 (2016) 52–76.
[13] R. Spotnitz, J. Franklin, J. Power Sources 113 (2003) 81–100.
[14] P. Verma, P. Maire, P. Novak, Electrochim. Acta 55 (2010) 6332–6341.
[15] Q.-F. Yuan, F. Zhao, W. Wang, Y. Zhao, Z. Liang, D. Yan, Electrochim. Acta 178 (2015) 682–688.
[16] D. Aurbach, E. Zinigrad, Y. Cohen, H. Teller, Solid State Ion. 148 (2002) 405–416.
[17] D. Aurbach, J. Power Sources 89 (2000) 206–218.
[18] F. Orsini, A. Du Pasquier, B. Beaudoin, J.M. Tarascon, M. Trentin, N. Langenhuizen, E. De Beer, P. Notten, J. Power Sources 76 (1998) 19–29.
[19] J.-G. Zhang, W. Xu, W.A. Henderson, Lithium Metal Anodes and Rechargeable Lithium Metal Batteries 249, Springer Series in Materials Science, 2017 (Chapter 2).
[20] (a) S. Takeda, W. Morimura, Y.-H. Liu, T. Sakai, Y. Saito, Rapid Commun. Mass Spectrom. 30 (2016) 1754–1762;
(b) V. Kraft, W. Weber, B. Streipert, R. Wagner, C. Shultz, M. Winter, S. Nowak, RSC Adv. 6 (2016) 8–17;
(c) C. Schultz, S. Vedder, M. Winter, S. Nowak, Anal. Chem. 88 (2016) 11160–11168.
[21] B.C. Church, D.T. Kaminski, J. Jiang, J. Mater. Sci. 49 (2014) 3234–3241.
[22] I. Doberdò, N. Löffler, N. Laszczynski, D. Cericola, N. Penazzi, S. Bodoardo, G.-T. Kim, S. Passerini, J. Power Sources 248 (2014) 1000–1006.
[23] M. Memm, A. Hoffman, M. Wohlfahrt-Mehrens, Electrochim. Acta 260 (2018) 664–673.